Development and simulation of isotropic hardening for AISI 1035 weld stress prediction during design and welding assembly of lower brackets of rail cars.

Available online at www.sciencedirect.com

ScienceDirect

Procedia CIRP 84 (2019) 916–922

www.elsevier.com/locate/procedia

29th CIRP Design 2019 (CIRP Design 2019)

Development and Simulation of Isotropic Hardening for AISI 1035 Weld Stress Prediction during Design and Welding Assembly of Lower Brackets of Rail Cars

*Daniyan, I. A.[a], Mpofu K.[a] , Fameso, F. O.[b], Adeodu, A. O. [c] and Bello, K. A. [c]

[a]*Department of Industrial Engineering, Tshwane University of Technology, Pretoria 0001, South Africa.**
[b]*Department of Industrial Engineering, Tshwane University of Technology, Pretoria 0001, South Africa.*
[c]*Department of Mechanical & Mechatronics Engineering, Afe Babalola University, Ado Ekiti, Nigeria.*
* Corresponding author. Tel.: +27 (064) 541-3537; *E-mail address:* afolabiilesanmi@yahoo.com

Abstract

Residual stresses through plastic deformation during the assembly operation of a rail car can cause cracks, distortion or other associated welding flaws if not checked. This study considers the use of analytical and numerical methods involving the simulation of isotropic hardening models for the prediction of AISI 1035 weld residual stresses during the arc welding assembly of the lower brackets of a rail car. Using the isotropic hardening model as well as the ABAQUS simulation software, the dynamic simulation of the gas metal arc welding process was performed at ambient temperature of 25°C over varying temperatures. The thermal modelling of the weld pass was carried out followed by the determination of the stress and strain values from the combined thermal elastic-plastic analysis. The results obtained indicated that the predictive ability of the isotropic model is highly significant, with the values of the weld stress and corresponding strain agreeing closely with the experimental values over varying ranges of temperatures. Hence, the isotropic hardening model can be used for weld residual stress simulation and prediction. Future work can consider the combination of both the isotropic and kinematic models.

Peer-review under responsibility of the scientific committee of the CIRP Design Conference 2019.

Keywords: Isotropic, Kinematic, Model, Simulation, Stress

1. Introduction

The thermo-elastic plastic analysis and changes in the micro structure of materials due to stress during welding is a complex process hence many researchers have reported the development of models and algorithms in finite element codes as well as dynamic simulation of welding operations for the prediction of weld residual stress [1-2]. Residual stresses are developed due to localized heating and non-uniform cooling accompanied with steep thermal gradients that arise in the weld zone. The detrimental effects of welding residual stresses on the structural integrity of welded structure are distortion, fatigue, failure of welded joints amongst others [3-6]. The determination of the transitional phase from elastic to plastic and to hardening states of a material often referred to as material's behaviour under the application of stress is essential in the design of welding processes where small dimensional changes due to stress or strain may significantly affect the structural integrity of the welded assembly. Also, the knowledge of the yield point under a constant or varying load is important because it determines the stress limit in order to avoid plastic flow

2212-8271 © 2019 The Authors. Published by Elsevier B.V.
Peer-review under responsibility of the scientific committee of the CIRP Design Conference 2019.
10.1016/j.procir.2019.04.297

during the design of welding operations. Zhou et al. [7] simulated the metal behaviours using different hardening models under cyclic loading, especially the nonlinear combined with the hardening model. Dormohammadi and Khoei [8] developed a three-invariant plasticity model based on a single-yield surface for the isotropic-kinematic hardening behaviour of granular materials focussing on the isotropic and kinematic hardening and dilation behaviours of material. Many works have also been reported on the isogeometric analysis of materials [9-21]. Guimares et al. [22] and Heinze et al. [23] investigated the amount and effect of residual stresses on materials during welding operations as well as the influencing factors using the numerical and physical experimentation method respectively. Wei et al. [24] characterized the heat affected zone as well as the mechanical properties for laser welding while Chen et al. [25] performed a finite element analysis of austenite decomposition during continuous cooling in 22MnB5 steel. Qin et al. [26] used the combined isotropic, kinematic and distortional hardening model to investigate aluminum and steels under complex strain-path changes. Other models have been developed to explain the transient changes that accompanies the strain path changes such as the crystal plasticity formulation [27-28] and continuum plasticity [29-30]. The practical application of all the models and dynamic simulation aforementioned for weld stress prediction during the welding assembly of the lower brackets of a rail car has not been sufficiently highlighted hence the aim of this work is to simulate the isotropic hardening models in order to predict the amount of weld stress during the welding assembly of the lower brackets of a rail car. This will bring about the prediction of the internal stresses of AISI 1035 during the welding operation of the rail car lower brackets. In addition, the simulation of the isotropic hardening model is essential in the determination of the elastic, plastic, stress and strain behaviour of AISI 1035 under varying loads and temperature.

2. Method

In this study, the Finite Element Analysis (FEA) was employed for developing the isotropic model while the hardening parameters were obtained from the physical experimentation test data.

For a multi-axis case, Equation 1 expresses the yield stress surface.

$$f_o(\sigma_{ij}) = 0 \quad (1)$$

On the other hand, the yield surface remains unchanged for a perfectly elastic surface as expressed by Equation 2.

$$f(\sigma_{ij}, k_i) = 0 \quad (2)$$

Where k_i represent the hardening parameters.

For the isotropic model, the load is assumed to be uniform and if the yield surface is symmetric about the stress axes, they remain equal as the yield surface develops with plastic strain. In the case of isotropic hardening, where the yield surface remains unchanged, but expands with increasing stress, Equation 3 holds;

$$f(\sigma_{ij}, k_i) = f_o(\sigma_{ij}) - k = 0 \quad (3)$$

The initial yield function determines the shape of the yield surface while the sizes changes with changes in the hardening parameter k. At the initial yield, the Von mises equation for yield surface holds as expressed by Equations 4a-c.

$$f_o(\sigma_{ij}) = \frac{1}{2}\sqrt{(\sigma_1 - \sigma_2)^2 + (\sigma_2 - \sigma_3)^2 + (\sigma_3 - \sigma_1)^2} - Y \quad (4a)$$

$$f_o(\sigma_{ij}) = \sqrt{3J_2} - Y \quad (4b)$$

$$f_o(\sigma_{ij}) = \sqrt{\frac{3}{2}S_{ij}} - Y \quad (4c)$$

Where Y is the yield stress in uniaxial tension.

For subsequent yielding, Equation 5 holds

$$f(\sigma_{ij}, k_i) = \sqrt{3J_2} - Y - k = 0 \quad (5)$$

The kinematic hardening model is useful when a hardening in tension leads to softening upon compression. Hence, the yield surface remains the same in shape and in size. The yield function is expressed by Equation 6.

$$f(\sigma_{ij}, k_i) = f_o(\sigma_{ij} - \alpha_{ij}) = 0 \quad (6)$$

Where α_{ij} is the shift stress hardening parameter

Considering the Von mises material for multi-axial case

$$f(\sigma_{ij}, k_i) = \sqrt{\frac{3}{2}(S_{ij} - \alpha_{ij}^d)(S_{ij} - \alpha_{ij}^d)} - Y = 0 \quad (7)$$

Where α^d is the deviatoric part of α and α_{ij} is the hardening parameter.

The mixed model, which combines the features of isotropic and kinematic model, is expressed as Equation 8.

$$f(\sigma_{ij}, k_i) = f_o(\sigma_{ij} - \alpha_{ij}) - k = 0 \quad (8)$$

The material functions include the plastic hardening modulus H and the isotropic hardening ratio β, hence, the material flow curve is expressed by Equation 9.

$$H = \frac{2}{3}\frac{d\sigma}{d\epsilon P} = \frac{2}{3}h_o(1 - \frac{\sigma}{\sigma^*})^q \quad (9)$$

Where; h_o, σ^*, q are the constants and σ is the yield stress.

The isotropic hardening incorporates both the hardening and softening function as expressed in Equation 10.

$$H_i = h_1 - h_2 \quad (10)$$

Hence H_i is determined from the tensile experiment.

The tensile back stress is expressed as Equation 11.

$$\sigma_b = \sigma_f + \sigma_r \quad (11)$$

Where; σ_f is the forward flow stress before reversing and σ_r is the reverse yield stress.

The back stress tensor B is deviatoric ($trB = 0$) hence

$$B_{11} = \frac{2}{3}\sigma_b = \frac{1}{3}(\sigma_f + \sigma_r) \quad (12)$$

The isotropic variables for monotonic loading is obtained by subtracting the back stress from the total stress (Equation 13).

$$S = \sigma - \frac{3}{2}B_{11} \quad (13)$$

Since $h_2 = 0$, for monotonic loading,

$$\dot{S} = h_{10}(1 - \frac{s}{\sigma^*})^q . \varepsilon_p \quad (14)$$

Equation 14 is integrated to obtain Equation 15.

$$S = S^* - [(S^* - S_0)^{(1-q)} + (q-1)\{h_{10}(S^*)^{-q})\varepsilon_p^{(\frac{1}{1-q})} \quad (15)$$

2.1 Finite element simulation

The weld stress prediction analysis conducted in this study employs the commercial finite element code ABAQUS ® to carry out of simplified modelling and simulation of isotropic hardening for a AISI 1035 weld assembly. The software code provides an environment for advanced linear and non-linear constitutive modelling and finite element analysis of thermo-mechanical and thermo-elastoplastic behaviour of engineering materials under different loading conditions. The model was built on the Complete Abaqus Environment (CAE), which provides the analysis tool ABAQUS/Standard that was used to model the initial thermal and mechanical loads, the dynamic response of the weld assembly to these loads and the subsequent final stress, strain and temperature profiles in the test piece. A combination of coupled thermal-displacement and mechanical loading steps where used to model the body heat flux and the short duration, high magnitude impact mechanical loading on the weld zone, similar to the simultaneous welding and peening operations associated with the assembly of lower brackets of rail cars. Two steps were defined, first, a coupled temperature-displacement step and then, a static general mechanical loading step into which the thermal load in the firsts step propagates. The weld zone was loaded with as is heat flux, corresponding to the weld temperature of 900 °C in the thermal step and then propagated into the mechanical loading step where a load of 5 kN was impacted on the top of the weld zone within a step time of 15 milliseconds. Both thermal and mechanical boundary conditions were imposed on the left and right sides on the x-axis of the assembly, to simulate the thermal relaxation and displacement constraints respectively, with the nodes on the sides subjected to conductive and encastre nodal displacement constrains. A C3D8RT mesh element of size 6mm, swept across the model part with advancing front as shown in Fig. 1c was used in meshing the model into finite elements before subjecting it to mathematical analysis. Results were produced within 360 seconds with a 32 GB, 3.2 GHz specification computer operating on Windows 7 OS version.

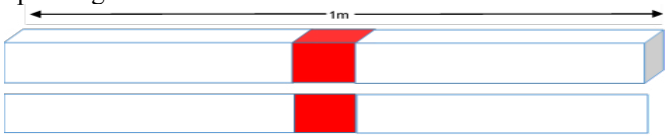

a. Unmeshed weld assembly

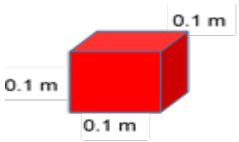

b. Weld zone.

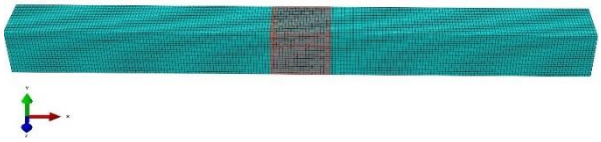

c. Meshed assembly

Fig. 1: Schematics of the weld assembly

2.2 Design against failure

In order to design against bending and eventual failure, the relation between the bending stress and the distance from the neutral horizon to guarantee safety must be obtained. From the simulation results outlined, the bending stress recorded in the test piece at the region of weld zone is approximately 496 MPa. From the load diagram shown in Fig. 2, the maximum bending moment M is expressed by Equation 16

$$M = maximum\ bending\ moment = \frac{WL}{4} \quad (16)$$

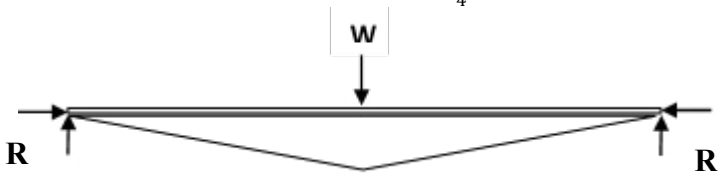

Fig. 2: Load diagram

$$Z = section\ modulus\ of\ the\ geometry = {}^{d^3}/_{6} \quad (17)$$

$$\delta_b = bending\ stress = {}^{M}/_{Z} = 496\ MPa = 496\ Nmm^{-2} \quad (18)$$

Where; $W = load = 5\ KN = 5000\ N$

$$L = lenght\ of\ the\ column = 1m = 1000\ mm$$

$$\delta_b = \left(\frac{\frac{WL}{4}}{{}^{d^3}/_{6}}\right) = \frac{6WL}{4d^3} \quad (19)$$

$d =$ The minimum distance from the neutral axis to guarantee safety shown in Fig. 3.

Fig. 3: Minimum distance from the neutral axis

$$d = \sqrt[3]{\frac{6WL}{4\delta_b}} = \sqrt[3]{\frac{6\times5000\times1000}{4\times496}} = 25\ mm$$

Recall; $\frac{\sigma}{y} = \frac{E}{R}$ (20)

Where; E and R are the Modulus of elasticity and allowable radius of curvature of the material respectively, both being material constants.

$$\therefore \frac{E}{R} = K \quad (21)$$

Let $\sigma = \delta_b$ and $y = d$

$$\delta_b = Kd \Rightarrow \delta_{b_1} = Kd_1 \Rightarrow \delta_{b_2} = Kd_2 \quad (22)$$

$$K = \frac{\delta_b}{d} = {}^{496}/_{25} = 19.8$$

Thus; $\delta_b = 19.8d$ (23)

Thus, the minimum distance from the neutral horizon to guarantee safety is obtained as 25 mm which implies that the minimum depth/thickness of the column which will withstand bending stress of up to 496 MPa without bending, distorting or failing should not be less than $2d$ i.e. 50 mm thickness. For bending stresses of higher magnitudes, Equation 23 provides a relation by which the minimum allowable thickness can be obtained.

2.3 Physical experimentation

The tensile test was used to measure the mechanical properties of the material; AISI 1035 AISI and relates the effect of a uniaxial tensile load on the extension of the standard specimen. The engineering stress and strain was thereafter calculated from the load-elongation data. The mechanical properties of carbon steel AISI 1035. The following materials and equipment were used: microscope fitted with a micrometer; Brinell hardness testing machine; heating furnace; The V-notched samples of AISI 1035 with varying thickness is shown in Fig. 4.

Fig. 4: V-notched AISI 1035 samples with varying thickness

The chemical properties of the carbon steel AISI 1035 whose density is 7850 kg/m^3 is presented in Table 1.

Table 1: The chemical composition of carbon steel AISI 1035

Fe	Mn	C	S	P
98.90	0.70	0.35	0.0050	0.0040

The mechanical and thermal properties of the specimen is presented in Tables 2 and 3 respectively.

Table 2: Mechanical properties of carbon steel AISI 1035

Properties	**Value**
Ultimate tensile strength	585 MPa
Yield strength	370 MPa
Modulus of elasticity	200 GPa
Bulk modulus	140 GPa
Shear modulus	80 GPa

Table 3: Thermal properties of AISI 1035 carbon steel

Thermal Properties	**Value**
Thermal expansion co-efficient (20°C)	11 µm/m°C
Thermal conductivity	51.9 W/mK

3. Results and Discussion

Fig. 5a-c show the plot of stress-strain whose data is obtained from the uniaxial tension test. There is a transient temperature change from the ambient 25°C to 900°C during the uniaxial tension test. Hence, an increase in temperature brings about plastic deformation, which significantly affects the stress-strain relationship under the applied load. Furthermore, in the uniaxial test case (one-dimensional), AISI 1035 will deform to the yield point and then harden. Once the value of the applied stress equals the yield strength of the material, plastic deformation will take place. A decrease in the value of the stress at the yield point results in elastic unloading while further increase in the value of the stress drives the plastic deformation to completion resulting in hardening. On the other hand, when the stress is held constant, no further plastic deformation or elastic unloading takes place.

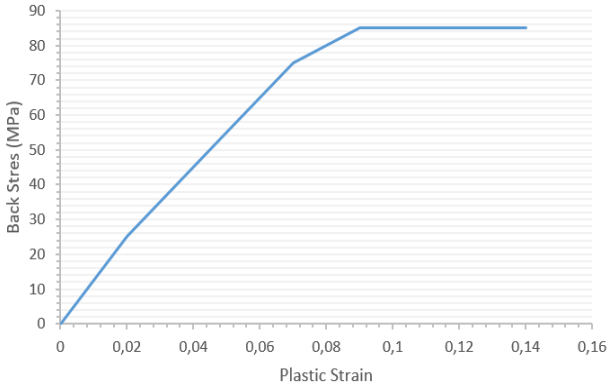

Fig. 5a: Plot of back stress-plastic strain

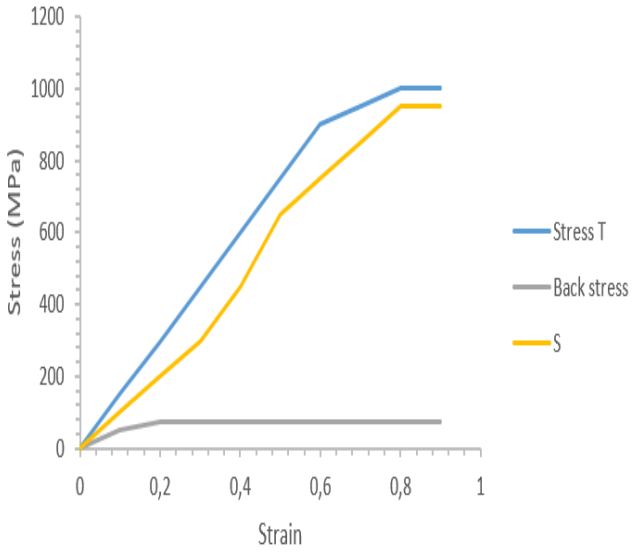

Fig. 5b: Uniaxial stress-strain

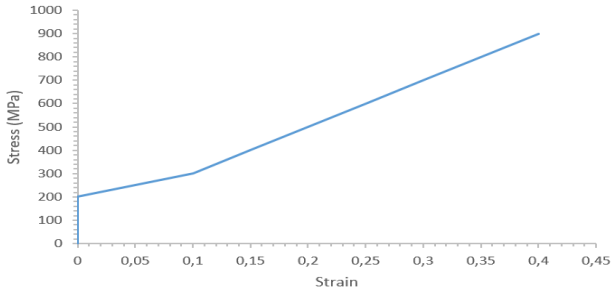

Fig. 5c: Stress-strain for reverse loading

3.1 Weld stress simulation

The results of the simulation of isotropic hardening model for the AISI 1035 weld assembly are shown in figures 7 to 11 with 3-D visualizations of the thermal distribution, surface residual stresses, distortion, strain profiles presented. For the purpose of this study, at various instances special focus will be placed on the magnified visualization of the profiles of the weld zone as shown in Figure 6, bearing in mind findings from previous studies which have shown that the weld zone experiences the most modifications to the microstructure of the assembly which in turn has effects on its intrinsic physical and mechanical properties.

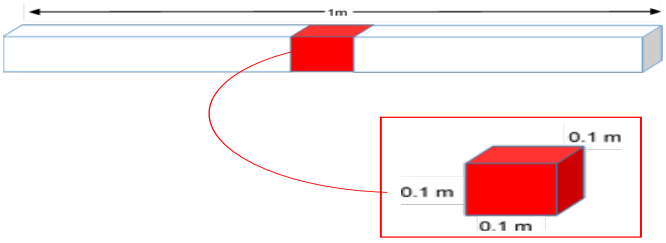

Fig. 6: Magnified view of the cross-section of the designated weld (affected) zone

Fig. 7 shows the magnitude of the overall stress distribution in the material during the simultaneous thermal and mechanical loading of the rail car bracket. The values of the maximum and minimum stress from Von Mises stress analysis of multi axial case type are obtained as 739.8 MPa and 8.08 MPa respectively, with the least stress recorded along the horizontal midriff of the column. Recall from table, the ultimate tensile strength (UTS) and yield strength (YS) of the material given as 550 MPa and 370 MPa respectively.

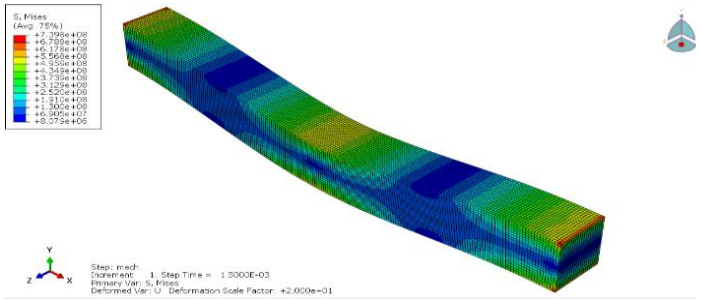

Fig. 7: Distribution of internal stresses

The magnitude of the maximum stress recorded in the test piece at the region of weld zone is approximately 496 MPa which indicates that the zone does experience some yield but however does not fail. Fig. 8 presents the surface stress distribution on the weld zone, shown as a magnified visualization of that region.

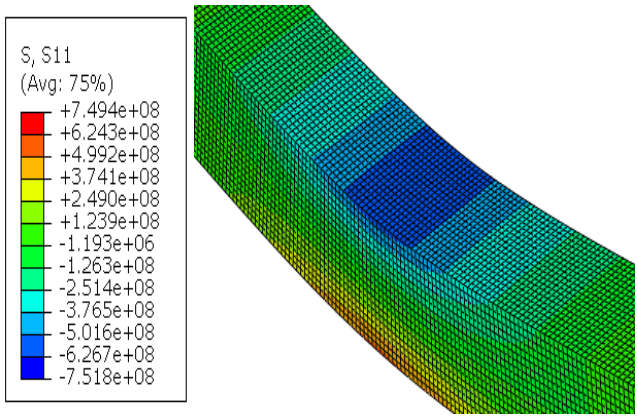

Fig. 8: Distribution of stresses across the x-axis (horizontal)

Comparing these values with that of the YS and UTS of the material, the maximum stress developed which (is compressive in nature) is between 500 – 630 MPa, exceeds the yield and ultimate strengths of the material. This is physically enough to produce actual plastic deformation of the material under the applied load. Precipitated by dislocation movements within the lattice and change in microstructure of the metal, the metal will eventually experience strain hardening on removal of the load. A larger fraction of the weld zone only experiences compressive stresses, which are less than the threshold stresses required for failure to occur. The symmetry of the surface across the stress axes is maintained as the plastic straining occurs. This is made evident by the surface distortions recorded, as presented in Fig. 9a-b. The mean distortion of the surface ranges from near zero along the x -axis (1.5 E-11) to absolute zero (0.00) along the z axis, an indication of a stationary origin of symmetry. This shows a fixed distortion at the origin with the yield surface expanding isotropically in both the x (0.062 mm right and left) and z (0.0078 mm forwards and backwards) direction.

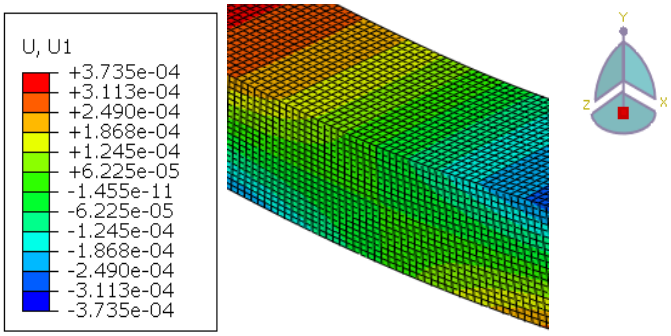

Fig. 9a: Nodal displacement profile across the x-axis (horizontal)

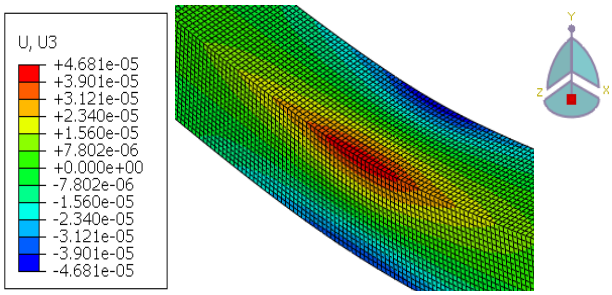

Fig. 9b: Nodal displacement profile across the z-axis (horizontal)

Quite interestingly, the top and bottom surfaces experience the highest strains as represented in Figure 10. This can largely be attributable to the hardening of the surfaces due to plastic deformation under application of stress during impact. Recall from Figure 8, that the stresses induced at the top surface is compressive in nature while those at the bottom is tensile. Notwithstanding, both top and bottom surfaces of the zone experience corresponding strains which indicates propensity for some permanent horizontal deformation of the top and bottom surfaces of the weld zone on impact. The thermal distribution of the assembly after impact is presented in Figure 11. The temperature dissipates axially across the assembly, when allowed to cool in air at room temperature, from the approximate weld temperature of 900 °C, with the thermal distribution remaining highest at the weld area at a temperature of 113.2 °C. This agrees significantly with the thermal conductivity of AISI 1035 at a maximum coefficient of thermal conductivity value of 51.9 W/m°C,

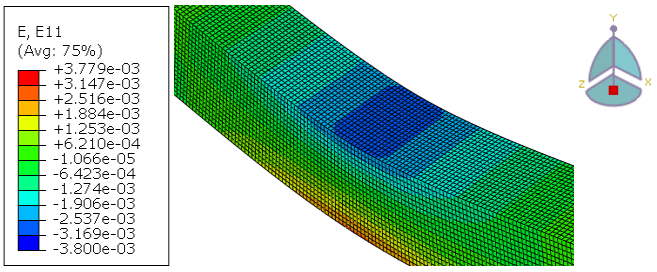

Fig. 10: Distribution of total strain on the x-axis (horizontal)

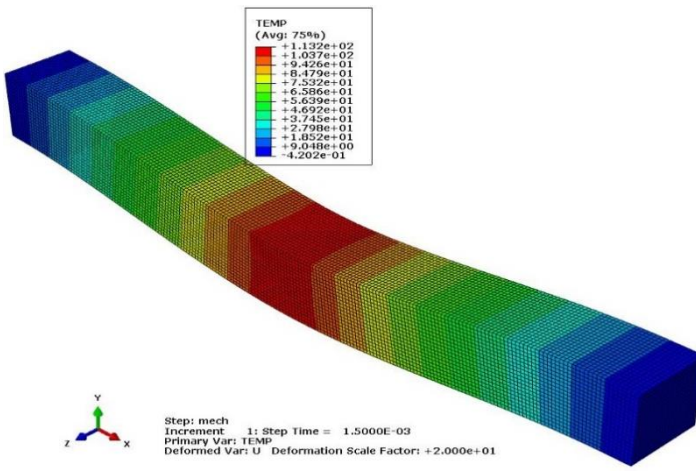

Fig. 11: Thermal distribution profile in the test piece

4. Conclusion

In this study, the simulation of the constitutive model of isotropic hardening has been successfully established for predicting the internal stresses of AISI 1035 rail car lower brackets weld assembly, such that the material hardening by pure isotropic hardening yields uniaxial thermal and mechanical response. The threshold stresses under which the material will deform or fail out rightly have been successfully investigated while the maximum allowable design load as well as the minimum allowable safe section thickness for brackets of similar dimensions, characteristics and properties to that used in the model have been defined. This work finds application in the rail car manufacturing industries during the welding assembly operations of the rail car components. Future work can consider the combination of both the isotropic and kinematic models.

References

[1] Ni, J. and Wahab, M. A. (2017). A numerical kinematic model of welding process for low carbon steels. Computers and Structures 186 (2017) 35–49.

[2] Deng D, Ma N, Murakawa H. A computational approach on prediction of welding residual stress with considering solid-state phase transformations. Trans JWRI 2012; 2011:79–82.

[3] Liu, C., Wang, C., Cheng, X., Yan, Y., Yang, J. and Guo,. Experimental Investigation on the Residual Stresses in a Thick Joint with a Partial Repair Weld Using Multiple-Cut Contour Method. Materials, 2018, 11(633)1-12.

[4] Zeinoddini, M., Arnavaz, S., Zandi, A. P. and Vaghasloo, Y. A. Repair Welding Influence on Offshore Pipelines Residual Stress Fields: An Experimental Study. J. Constr. Steel Res. 2013, 86:31–41.

[5] Hernandez, A. I., Aguilera, G. E. and Perez, M. J. Welding Sequence Analysis in Three Dimensional Weldments with Experimental Verification. MEMORIAS DEL XXII CONGRESO DE LA SOMIM DEL 28 AL 30 DE SEPTIEMBRE DEL 2016 CD. MÉRIDA, YUCATÁN. MÉXICO, 2016, pp. 376-387.

[6] Song, S. and Dong, P. Residual Stresses at Weld Repairs and Effects of Repair Geometry. Sci. Technol. Weld. Join. 2017, 22:265–277.

[7] Zou, Y., Yun, G., Zhuang, Z., Kasa, S. and Tsunori, M. Development of Combined Hardening Model for the Metal Material under Cyclic Loading, International Journal for Computational Methods in Engineering Science and Mechanics, 2007, 8(4):181-187.

[8] DorMohammadi, H. and Khoei, A. R. A single plasticity model with isotropic–kinematic hardening rule for granular materials. International Journal of Solids and Structures, 2015, pp. 1-37.

[9] Tu, H. Y., Schmauder, S., Weber, U., Rudnik, Y. and Ploshikhin V. Simulation of the damage behaviour of electron beam welded joints with the Rousselier model. Eng. Fract. Mech. 2013; 103:153–161.

[10] Nguyen, V. P., Anitescu, C., Bordas, S. P. A., Rabczuk, T. Isogeometric analysis: an overview and computer implementation aspects. Math. Comput. Simul. (MATCOM) 2015; 117(issue C):89–116.

[11] Nguyen-Thanh, N., Valizadeh, N., Nguyen, M. N., Nguyen-Xuan, H., Zhuang, X., Areias, P. An extended isogeometric thin shell analysis based on Kirchhoff-Love theory. Comput. Methods Appl. Mech. Eng. 2015; 284:265–291.

[12] Thai, T. Q., Rabczuk, T., Bazilevs, Y., Meschke, G. A higher-order stress-based gradient-enhanced damage model based on isogeometric analysis. Comput. Methods Appl. Mech. Eng. 2016; 304:584–604.

[13] Anitescu, C., Jia, Y., Zhang, Y. J., Rabczuk, T. An isogeometric collocation method using superconvergent points. Comput. Methods Appl. Mech. Eng. 2015; 284:1073–1097.

[14] Phung, V., P., Qui, L. X., Nguyen-Xuan, H., Wahab, M. A. Size-dependent isogeometric analysis of functionally graded carbon nanotube-reinforced composite nanoplates. Compos. Struct. 2017; 166:120–135.

[15] Tran, L. V., Phung-Van, P., Lee, J., Wahab, M. A., Nguyen-Xuan, H.

Isogeometric analysis for nonlinear thermomechanical stability of functionally graded plates. Compos. Struct. 2016; 140:655–667.
[16] Nguyen, H. X., Nguyen, T. N., Abdel Wahab, M., Bordas, S. P. A., Nguyen-Xuan, H., Voa, T. P. A refined quasi-3D isogeometric analysis for functionally graded microplates based on the modified couple stress theory. Comput. Methods Appl. Mech. Eng. 2017; 313:904–940.
[17] Thai, C. H., Ferreira, A. J. M. Abdel Wahab, M., Nguyen-Xuan, H. A generalized layerwise higher-order shear deformation theory for laminated composite and sandwich plates based on isogeometric analysis. Acta Mech. 2016; 227 (5):1225–1250.[18] Tran, V. L., Lee, J., Nguyen-Van, H., Nguyen-Xuan, H., Abdel Wahab, M. Geometrically nonlinear isogeometric analysis of laminated composite plates based on higher-order shear deformation theory. Int. J. of Non-Linear Mech. 2015; 72:42–52.
[19] Phung, V. P., Tran, L. V., Ferreira, A. J. M. Nguyen-Xuan, H., Abdel-Wahab, M. Nonlinear transient isogeometric analysis of smart piezoelectric functionally graded material plates based on generalized shear deformation theory under thermo-electro-mechanical loads. Nonlinear Dyn. 2016:1–16.
[20] Phung, V. P., De Lorenzis, L., Thai, C. H., Abdel Wahab, M., Nguyen-Xuan, H. Analysis of laminated composite plates integrated with piezoelectric sensors and actuators using higher-order shear deformation theory and isogeometric finite elements. Comput Mater Sci. 2015; 96:495–505.
[21] Thai, C., Zenkour, A. M., Abdel Wahab, M., Nguyen-Xuan, H. A simple four-unknown shear and normal deformations theory for functionally graded isotropic and sandwich plates based on isogeometric analysis. Compos. Struct. 2016; 139:77–95.
[22] Guimares, P. B., Pedrosa, P. M. A., Yadava, Y. P., Barbosa, J. M. A., Filho, A. V. S., Ferreira, R. A. S. Determination of residual stresses numerically obtained in ASTM AH36 steel welded by TIG process. Mater. Sci. Appl. 2013; 04(04):7.
[23] Heinze, C., Pittner, A., Rethmeier, M., Babu, S. S. Dependency of martensite start temperature on prior austenite grain size and its influence on welding induced residual stresses. Comput. Mater. Sci. 2013; 69:251–260.
[24] Wei, C. H., Zhang, J., Yang, S. L., Tao, W., Wu, F. S., Xia, W. S. Experiment-based regional characterization of HAZ mechanical properties for laser welding. Int. J. Adv. Manuf. Technol. 2015; 78(9–12):1629–1640.
[25] Chen, X., Xiao, N., Li, D., Li, G., Sun, G. The finite element analysis of austenite decomposition during continuous cooling in 22MnB5 steel. Modell. Simul. Mater. Sci. Eng. 2014; 22(6):065005.
[26] Quin, J., Holmedal, B. and Hopperstad, O. S. A combined isotropic, kinematic and distortional hardening model for aluminum and steels under complex strain-path changes. International Journal of Plasticity, 101 (2018) 156–169.
[27] Wen, W., Borodachenkova, M., Tomé, C. N., Vincze, G., Rauch, E. F., Barlat, F., Grácio, J. J.,Mechanical behavior of Mg subjected to strain path changes: experiments and modeling International Journal of Plasticity, 2015, 73, 171–183.
[28] Wen, W., Borodachenkova, M., Tomé, C. N., Vincze, G., Rauch, E. F., Barlat, F., Grácio, J. J. Mechanical behavior of low carbon steel subjected to strain path changes: experiments and modeling. Acta Mater. 2016, 111, 305–314.
[29] Barlat, F., Vincze, G., Grácio, J. J., Lee, M.-G., Rauch, E. F., Tomé, C. N. Enhancements of homogenous anisotropic hardening model and application to mild and dual-phase steels. International Journal of Plasticity, 2014, 58, 201–218.
[30] Mánik, T., Holmedal, B. and Hopperstad, O. S. Strain-path change induced transients in flow stress, work hardening and r-values in aluminum. International Journal of Plasticity, 2015, 69, 1–20.